

## First Measurements of High Frequency Cross-Spectra from a Pair of Large Michelson Interferometers

Aaron S. Chou,<sup>1</sup> Richard Gustafson,<sup>2</sup> Craig Hogan,<sup>1,3</sup> Brittany Kamai,<sup>3,4</sup> Ohkyung Kwon,<sup>3,5</sup> Robert Lanza,<sup>3,6</sup>  
Lee McCuller,<sup>3,6</sup> Stephan S. Meyer,<sup>3</sup> Jonathan Richardson,<sup>3</sup> Chris Stoughton,<sup>1</sup> Raymond Tomlin,<sup>1</sup>  
Samuel Waldman,<sup>7</sup> and Rainer Weiss<sup>6</sup>

(Holometer Collaboration)

<sup>1</sup>*Fermi National Accelerator Laboratory, Batavia, Illinois 60510, USA*

<sup>2</sup>*University of Michigan, Ann Arbor, Michigan 48109, USA*

<sup>3</sup>*University of Chicago, Chicago, Illinois 60637, USA*

<sup>4</sup>*Vanderbilt University, Nashville, Tennessee 37235, USA*

<sup>5</sup>*Korea Advanced Institute of Science and Technology (KAIST), Daejeon 34141, Republic of Korea*

<sup>6</sup>*Massachusetts Institute of Technology, Cambridge, Massachusetts 02139 USA*

<sup>7</sup>*SpaceX, Hawthorne, California 90250, USA*

(Received 9 May 2016; published 9 September 2016)

Measurements are reported of the cross-correlation of spectra of differential position signals from the Fermilab Holometer, a pair of colocated 39 m long, high power Michelson interferometers with flat broadband frequency response in the MHz range. The instrument obtains sensitivity to high frequency correlated signals far exceeding any previous measurement in a broad frequency band extending beyond the 3.8 MHz inverse light-crossing time of the apparatus. The dominant but uncorrelated shot noise is averaged down over  $2 \times 10^8$  independent spectral measurements with 381 Hz frequency resolution to obtain  $2.1 \times 10^{-20} \text{ m}/\sqrt{\text{Hz}}$  sensitivity to stationary signals. For signal bandwidths  $\Delta f > 11 \text{ kHz}$ , the sensitivity to strain  $h$  or shear power spectral density of classical or exotic origin surpasses a milestone  $\text{PSD}_{\delta h} < t_p$  where  $t_p = 5.39 \times 10^{-44} / \text{Hz}$  is the Planck time.

DOI: [10.1103/PhysRevLett.117.111102](https://doi.org/10.1103/PhysRevLett.117.111102)

In this Letter, we report first data from a pair of colocated and coaligned 39.06 m long power-recycled Michelson interferometers, each operating at 2 kW power with mean shot-noise-limited differential position noise sensitivity of  $2.1 \times 10^{-18} \text{ m}/\sqrt{\text{Hz}}$ . The apparatus adopts many of the technologies developed for sub-kHz gravitational wave detection [1–6] but is instead optimized for a much larger signal bandwidth extending up to 25 MHz. Whereas gravitational wave interferometers incorporate Fabry-Perot arm cavities and/or an output port recycling cavity to resonantly enhance the instrumental response to differential strain at low frequencies, the new interferometers employ only common mode power recycling cavities and, thus, do not low-pass filter the differential signals. They, thus, maintain their full Michelson differential bandwidth at frequencies up to the 3.8 MHz inverse light-crossing time of the apparatus [7]. The signal fluctuations in interference fringe power are digitized at 50 MHz to achieve a detection bandwidth much larger than that of typical gravitational wave detectors. While some prototype resonant detectors have been operated at such high frequencies [8–10], the broadband strain sensitivity of the new instrument far exceeds that of previously reported narrow band results at these frequencies. Moreover, similar to GEO600 [6,11]

but unlike LIGO [4], the full recycled laser power of each new interferometer is incident on the beam splitter, thus, giving equal sensitivity to longitudinal strain and to transverse shear fluctuations, as measured relative to the laser beam propagation direction in each interferometer arm.

A large improvement in sensitivity to external but local stationary signals common to both interferometers is achieved by cross-correlating the outputs of the two devices to average away uncorrelated noise. While this interferometer cross-correlation technique has been demonstrated by the LIGO Scientific Collaboration [12–15], the higher frequency signal band of the Holometer enables two significant improvements in noise reduction. First, while LIGO has operated two colocated interferometers H1 and H2 in the same vacuum system at the Hanford site, the cross-correlation analysis has been complicated by substantial contributions of correlated environmental noise at low frequencies. In contrast, the  $f \gtrsim 1 \text{ MHz}$  signal band of the new instrument is largely free of this low frequency seismic and acoustic noise. Second, the enhanced signal bandwidth, as large as  $\Delta f = 25 \text{ MHz}$  (compared to the  $< 1 \text{ kHz}$  bandwidth of typical gravitational wave detectors) reduces the time required per independent measurement and, thus, enables a much larger noise averaging factor

$\sqrt{N_{\text{meas}}} = \sqrt{\tau_{\text{int}} \Delta f}$  for any cumulative integration time  $\tau_{\text{int}}$ . In an example described below, the new spectral data are analyzed to test a speculative model of Planckian diffraction, and the noise is averaged down by a factor of  $\sqrt{(145 \text{ h})(700 \text{ kHz})} \approx 6 \times 10^5$ . The data constrain strain or shear power spectral density in the detection band to be  $\text{PSD}_{\delta h} < 0.25 \times t_p$  where  $t_p = 5.39 \times 10^{-44}/\text{Hz}$  is the Planck time.

*Experimental design.*—In each interferometer, continuous wave  $\lambda = 1064 \text{ nm}$  laser light is injected to a beam splitter, divided into two orthogonal arms, and reflected at distant end mirrors. The returning beams coherently interfere at the beam splitter, with intensity varying as  $P_{\text{fringe}} = P_{\text{BS}}[\epsilon_{\text{CD}} + (1 - 2\epsilon_{\text{CD}})\sin^2(2\pi X/\lambda)]$  at the antisymmetric port. In this expression, the differential arm length (DARM) is given by  $X \equiv L_1 - L_2$  where  $L_1 \approx L_2 = 39.06 \text{ m}$  is the length of the two arms. Perturbations  $\delta X$  due to either strain or shear are imprinted as amplitude modulation on the output fringe power.  $P_{\text{BS}}$  is the power incident on the beam splitter, and the contrast defect parameter  $\epsilon_{\text{CD}}$  characterizes residual leakage of noninterfering light caused by geometrical mismatches in the beams returning from the two arms.

The remaining power exiting the symmetric beam splitter port and returning towards the laser is instead reflected back into the device using a 1000 ppm transmission mirror. The insertion of this input coupling mirror forms an overcoupled Fabry-Perot cavity with free spectral range  $\text{FSR} \approx 3.8 \text{ MHz}$  determined by the common arm length  $(L_1 + L_2)/2$ . The laser is frequency locked to the instantaneous cavity frequency via the Pound-Drever-Hall (PDH) technique [16,17] to achieve a typical power buildup from the injected 1.1 W laser power to intracavity power  $P_{\text{BS}} \approx 2 \text{ kW}$  into the beam splitter from the recycling mirror. The 900 Hz transmission bandwidth of the optical cavity filters higher frequency amplitude and phase noise present on the incident laser beam. It also indicates a total of  $\approx 1470$  ppm round-trip loss including recycling transmissivity, scattering or absorption losses, Michelson fringe offset, and defect leakage.

To produce a linear response to differential length perturbations  $\delta X$ , each interferometer is operated at a DARM offset of around 1 nm from a dark fringe. No optic is suspended, but steel and Viton spring stacks damp environmental noise above 15 Hz. A digital control system monitors fluctuations in the output light and feeds back differential signals to piezoelectric actuated end mirror mounts to hold the fringe offset within the 700 Hz unity gain frequency. The shaped loop maintains a 50 pm rms residual motion as measured through the 16 kHz control system Nyquist frequency. Narrow band excitations used for length sensitivity calibration and alignment control account for half of this rms. At this fringe offset, around 50 ppm of signal-bearing interference light appears at the antisymmetric port, as measured relative to the intracavity power. This value is chosen to balance the interference

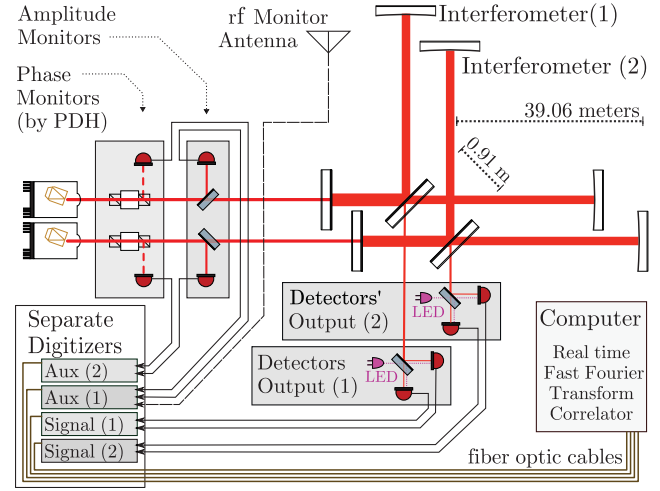


FIG. 1. Schematic of the two colocated interferometers and associated data acquisition channels. The two devices are optically and electrically isolated to eliminate cross talk.

fringe light with the noninterfering contrast defect light leakage  $\epsilon_{\text{CD}} \approx 50 \text{ ppm}$ , which carries no signal but contributes shot-noise variance.

Accounting for detection inefficiencies and contrast defect degradation, the mean shot-noise-limited displacement sensitivity due to the 2 kW power incident on the beam splitters is  $\text{PSD}_{\delta X}^{\text{shot}} \approx (2.1 \times 10^{-18} \text{ m}/\sqrt{\text{Hz}})^2$ ; the excess power spectral density compared to an ideal 2 kW Michelson is  $2.1\times$  in one machine and  $3.5\times$  in the other. These sensitivities are confirmed by calibration measurements as summarized below. The signals from the two interferometers are cross-correlated and averaged to reach sensitivity more than 4 orders of magnitude below the shot-noise limit.

The success of the cross-correlation averaging technique depends on low instrumental correlation between the two interferometers and requires nearly complete independence of the two devices, despite sharing an experimental hall. Each interferometer is enclosed in its own vacuum system, and the injection and control systems are operated on separate optics tables and electronics racks. The digitizers for the two instruments are isolated and independently synchronized to Global Positioning System, communicating with the real-time spectrum processing computer only through optical fiber (see Fig. 1).

*Data acquisition and methodology.*—Two-hundred mW of detected asymmetric port power in each interferometer is required to balance between photodiode limits and excess noise from contrast defect. The large dynamic range between this dc power and the shot-noise level presents challenges for linear detection. The output power is split by a secondary beam splitter to divide it between two custom low transimpedance photoreceivers based on high linearity, 2 mm InGaAs photodiodes. This linearity is demonstrated in each detector with dc power up to 150 mW. A low gain dc amplification channel samples the photocurrent and has

flat response from dc-80 kHz. A high gain, transimpedance-based, ac-coupled radio frequency (rf) channel is best calibrated between 900 kHz and 6 MHz and digitizes to a 25 MHz Nyquist frequency. Outside this band, the phase matching of the calibration deteriorates, impacting the real projection of the complex cross-correlation.

The two interferometers together, thus, have four rf output streams, each digitized at 100 MHz sample rate with 14 bits and then downsampled to 50 MHz. These four channels along with an additional four auxiliary monitor channels are fast Fourier transformed in real time with 381 Hz frequency resolution. A symmetric  $8 \times 8$  cross-spectrum matrix is computed. The real-time computation rate limits the digitization to 50 MHz. Measurements of these 36 (cross-) spectra are averaged over 700 sequential spectral measurements (around 1.8 s) for storage. The remaining averaging is performed in off-line analysis.

Isolation of the two interferometers is established by measurement, as described below in the backgrounds section. During the accumulation for this result, the auxiliary channels are set at various times to monitor the PDH laser phase noise, the laser intensity noise, and loop antennas detecting the local rf environment.

*Absolute calibration of sensitivity.*—An indirect calibration ladder is used to establish the instantaneous length sensitivity at MHz frequencies. Because of resonances in the piezo stacks actuating the end mirrors, a mechanical dither signal can only be injected at a low frequency of 1 kHz, whereas the rf detector channel is high-passed at 900 kHz. The 1 kHz dither is calibrated by misaligning the cavity mirrors to operate the interferometers in a non-power-recycled configuration with a simple Michelson response. The end mirrors are then slowly actuated to sweep across an entire interference fringe to reference the voltage signal to the 1064 nm wavelength. After correcting for the measured interferometer control system feedback, the *in situ* dither amplitude is determined to be  $10^{-11}$  m. Measurements of the low-passed dc and the high-passed rf transfer functions of the photoreceivers refer the 1 kHz length-calibrated *in situ* dither to the signal band above 1 MHz with 5% systematic uncertainty. The resulting calibration matches the sensitivity expected from fitted interferometer parameters of cavity power, contrast defect, and the DARM fringe offset fit using slow controls data of the calibration lines and readouts of the asymmetric port, arm transmission power, and cavity reflection power.

*In situ monitoring of data quality.*—During data-taking operations, the 1 kHz DARM dither is run continuously. For each detector, both the dc photocurrent and the 1 kHz signal are monitored from the detector dc channel, and the ratio of these measures is a proxy for the instantaneous fringe offset. The shot-noise level in the 1–2 MHz signal band is also continuously monitored, and the ratio of this to the dc photocurrent signal monitors the relative stability of the photoreceiver rf and dc channel responses. These and other observables such as the power reflected from the

cavity back towards the laser and the power transmitted through the end mirrors serve to monitor the stability of the calibrated sensitivity of the instrument to position disturbances. The uncertainty in calibration from both systematic uncertainties and run-to-run variability is less than 10%.

Periods with abnormal operating conditions are vetoed prior to accumulation into the averaged spectra. To verify the control system lock to a stable fringe offset, the low frequency photocurrent is continuously monitored and periods of lock loss are rejected. Periods of enhanced rf noise exceeding shot noise by 20% are also rejected. Fast noise glitches are identified by a threshold veto on the raw time-series photocurrent data, preventing analog-to-digital converter clipping. During transition periods when the control system lock of the interferometer is lost or is being reacquired, 4 s of data immediately before the lock loss and immediately after a lock reacquisition are vetoed. During active data taking, the duty cycle for stable operations is greater than 80%.

To monitor the timing stability of the cross-correlation data acquisition system, separate light-emitting diode (LED) flashers driven from a common source inject a 13 MHz timing calibration line to the output photodiodes. The LED signal amplitude and phase coherence in each detector is continuously recorded and indicates that the electronically isolated digitizers have high phase stability for frequencies up to 25 MHz.

*Measured spectra.*—Figure 2 shows the measured auto- and cross-spectra averaged over 145 h of data taken in July and August, 2015. The autospectrum for each individual interferometer is obtained by a weighted average of its two output photodetectors, with weighting given by the instantaneous calibrated DARM sensitivity. The many subsequent measurements are also similarly weighted when summed into the average. The raw 381 Hz resolution spectra are frequency averaged to produce spectra with 3.81 kHz resolution and negligible bin-to-bin correlation. At high frequencies, these spectra are shot-noise limited as expected with flat regions well described by Gaussian noise. A repeating sequence of peaks is due to thermally excited acoustic modes of individual optics substrates. The magnitude of the resolved acoustic lines is consistent with that expected from the ambient temperature. Excess power is also seen at higher order mode resonances of the Fabry-Perot cavity for each interferometer and at the 3.8 MHz FSR. At these resonances, the amplitude and phase noise of the laser are no longer efficiently filtered by the cavity, and leak through to the output port. Because the interferometers use independent optics and lasers, the excess noise from these sources is uncorrelated but reduces the sensitivity of the experiment at affected frequencies.

The measured cross-spectral data are projected onto the real axis to search for correlation at zero time delay. The shot-noise-limited measured power is consistent with the expected statistical sensitivity with  $\sqrt{N_{\text{spectra}}}$  improvement from averaging. The data are verified to be normally distributed with no statistically significant outliers.

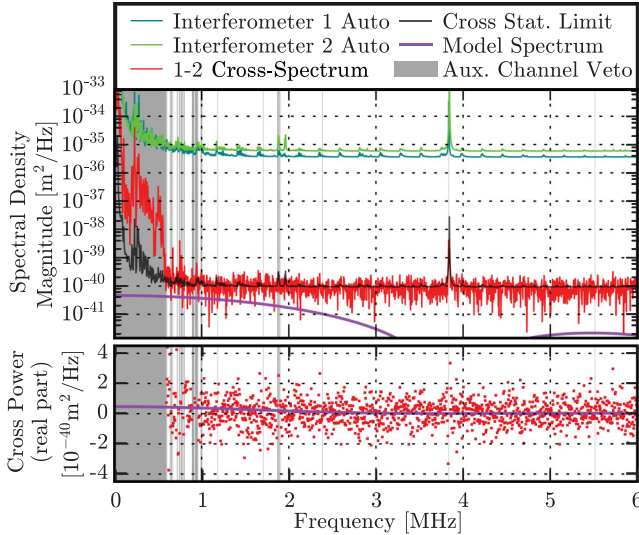


FIG. 2. Accumulated power spectra with 3.81 kHz resolution enlarged to frequencies near the free spectral range. In the upper panel, the two upper curves show the output PSD (averaged over the two photodetectors) for each interferometer. Below that are two curves showing the expected noise in the cross-correlation based on  $\sqrt{N_{\text{spectra}}}$  averaging of the PSDs and the observed magnitude of the cross-correlation data. The lower panel plot is on a linear scale and is the real part of the cross-correlation spectrum. This is the signal integrated in Fig. 3. Both panels also show an example broadband model spectrum with Planckian normalization as given by Eq. (1).

**Backgrounds and frequency bin vetoes.**—A limited set of potential backgrounds is studied in order to constrain the possible destructive interference of environmental contamination with a putative signal spectrum. The laser phase and amplitude noise spectra are measured *in situ* via optical pickoffs prior to injection and recorded in the auxiliary rf channels. The cross-spectra of these channels with the interferometer output channels is calibrated using *ex situ* transfer function measurements. At frequencies below 1 MHz, the interferometer output spectra are dominated the  $1/f$  laser phase noise, incompletely suppressed by the cavity filter. Frequency bins with high coherence to the laser phase and amplitude monitors of the opposite interferometer, or with external antenna channels, are vetoed for the analysis. Data below 100 kHz are vetoed due to a large environmental noise component, while the auxiliary channels enforce vetoes at frequencies up to 600 kHz and sporadically above that. These vetoes rely only on auxiliary channels and do not systematically bias the search for signal power in the interferometer output. Vetoed regions are shaded in gray in the plots. For remaining bins, correlated or anticorrelated laser noise is statistically limited to be  $< 3\%$  of the estimated Planckian power spectrum. Furthermore, dark noise studies indicate correlated electronic pickup and environmental light (including the LED timing calibrators) to be  $< 1\%$  of the statistical sensitivity.

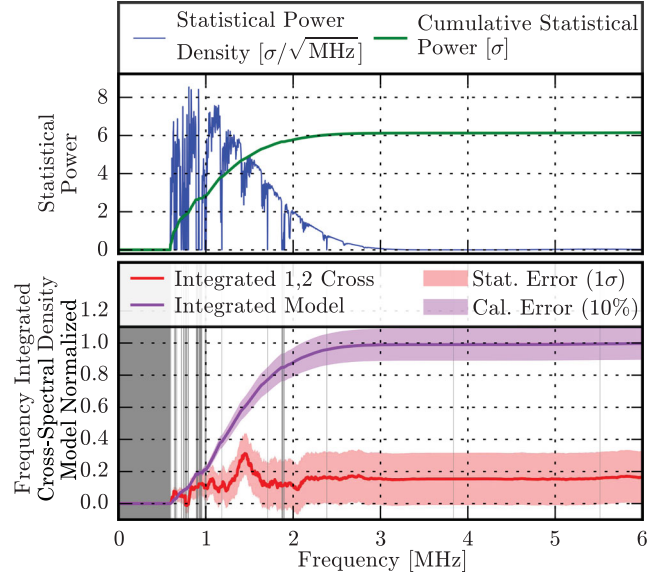


FIG. 3. The upper panel shows the predicted measurement significance (model signal or instrument noise) in each frequency bin as well as its integral. The lower panel shows the frequency integrated measurement with a shaded  $1\sigma$  uncertainty limit along with the integrated model spectrum. Both are normalized to the predicted model amplitude. The shaded region around the model curve is the 10% calibration uncertainty. The gray bands are frequencies vetoed using ancillary and housekeeping data.

**Model testing.**—As an example of how the spectral data can be used, we consider a speculative model in which irreducible space-time noise arising from a putative fundamental Nyquist frequency  $f_p = 1/t_p$  grows via diffraction over macroscopic distances to give a white noise shear power spectral density quantitatively equal to  $t_p$ . In units of position variance, the predicted power spectral density (plotted as the purple curve in Fig. 2) takes the following representative form [18]:

$$\text{PSD}_{\delta x}(f) = \frac{t_p}{\sqrt{\pi}} L^2 \frac{\sin^2(\pi(2L/c)f)}{(\pi(2L/c)f)^2}, \quad (1)$$

which is a sinc response function normalized to  $4.64 \times 10^{-41} \text{ m}^2/\text{Hz}$  and distributed over the 3.8 MHz free spectral range for arm length  $L \approx 39 \text{ m}$ . While this space-time noise is expected to be correlated between colocated interferometers, the decoherence due the small separation  $d = 0.91 \text{ m}$  between the two beam splitters would cause a  $d/L = 2.3\%$  reduction in the normalization of the model cross-spectrum.

To optimize sensitivity to the predicted spectral shape, each nonvetoed 3.81 kHz bin is weighted by the (predicted) signal-to-noise ratio with signal estimated from the model spectrum Eq. (1) and noise variance estimated from the measured interferometer autospectra divided by  $\sqrt{N_{\text{spectra}}}$ . Figure 3 shows this result in the form of a weighted frequency integral of the cross-spectrum data from Fig. 2. Plotted on the upper panel of Fig. 3 is the measurement weight shown as a potential signal significance density for

each frequency bin ( $\sigma/\sqrt{\text{MHz}}$ ). As discussed above, the shot noise is exceeded at some frequencies by other uncorrelated stochastic noise sources causing dips in the expected significance density which reduce the instrument's integrated sensitivity by about 10% while causing no systematic bias. For this model, about 20% of the potential signal significance comes from frequencies below 1 MHz, 70% from frequencies between 1 and 2 MHz, and 10% from above 2 MHz. The integrated significance shows the potential for  $6.2\sigma$  statistical sensitivity for detecting or rejecting this model.

The lower panel of Fig. 3 shows the frequency integral of the predicted signal given in Eq. (1) weighted by the expected signal-to-noise ratio. This curve is normalized to integrate to unity with a shaded band representing the 10% calibration uncertainty. The lower curve in this plot is the corresponding integral of the weighted data points. This curve exhibits a random walk, thus, indicating that the significance accumulation has no excessive contribution from any particular frequency band. The integral takes into account the small correlations between adjacent frequency bins due to apodization and sampling. The shaded vertical bands are vetoed regions as described above. The end point to the right of the plot is the total integrated signal and is the result of this analysis. The shaded band around the curve is the  $\pm 1\sigma$  accumulated statistical uncertainty.

Using all data up to 25 MHz, the weighted integral curve remains statistically consistent at  $1.1\sigma$  with zero broadband correlation. The model of Eq. (1) is, thus, excluded with  $5.1\sigma$  statistical significance, reduced by the 10% calibration uncertainty to  $4.6\sigma$ . Alternatively, the result may be viewed as a constraint on the normalization of this model to be less than 44% of the predicted value at 95% confidence level. It should be emphasized that these results apply only to the spectral shape of the particular model used here. Similar analysis techniques should be used for testing of any model which predicts shear or strain variance power in this detection band.

*Conclusions.*—Modern interferometers including the ones described here are now achieving correlated strain sensitivity surpassing Planckian normalization and, thus, may provide data useful for searching for new effects potentially arising from Planck scale microphysics. Further studies will survey with improved sensitivity other potential models with possible Planckian information content accessible to the current instrument [19]. These measurements will also provide uniquely deep constraints on gravitational waves in the MHz band. While the apparatus in its current Michelson layout is equally sensitive to shear and strain noise, it would not respond to correlated exotic noise power in rotational observables; these could be studied with a similar instrument reconfigured with bent arms [20].

This work was supported by the Department of Energy at Fermilab under Contract No. DE-AC02-07CH11359 and the Early Career Research Program (FNAL FWP 11-03), and by

grants from the John Templeton Foundation, the National Science Foundation (Grants No. PHY-1205254, No. DGE-0909667, No. DGE-0638477, and No. DGE-1144082), NASA (Grant No. NNX09AR38G), the Fermi Research Alliance, the Ford Foundation, the Kavli Institute for Cosmological Physics, University of Chicago/Fermilab Strategic Collaborative Initiatives, and the Universities Research Association Visiting Scholars Program. The Holometer team gratefully acknowledges the extensive support and contributions of Bradford Boonstra, Benjamin Brubaker, Marcin Burdzy, Herman Cease, Tim Cunneen, Steve Dixon, Bill Dymond, Valera Frolov, Jose Gallegos, Hank Glass, Emily Griffith, Hartmut Grote, Gaston Gutierrez, Evan Hall, Sten Hansen, Young-Kee Kim, Mark Kozlovsky, Dan Lambert, Scott McCormick, Erik Ramberg, Doug Rudd, Geoffrey Schmit, Alex Sippel, Jason Steffen, Sali Sylejmani, David Tanner, Jim Volk, William Wester, and James Williams for the design and construction of the apparatus.

- 
- [1] R. Weiss, *Qtr. Prog. Rep.* **105**, 54 (1972).
  - [2] P. Saulson, *Fundamentals of Interferometric Gravitational Wave Detectors* (World Scientific, Singapore, 1994), ISBN .
  - [3] B. P. Abbott *et al.* (LIGO Scientific Collaboration), *Rep. Prog. Phys.* **72**, 076901 (2009).
  - [4] R. X. Adhikari, *Rev. Mod. Phys.* **86**, 121 (2014).
  - [5] W. Winkler, K. Danzmann, H. Grote, M. Hewitson, S. Hild, J. Hough, H. Lück, M. Malec, A. Freise, K. Mossavi *et al.*, *Opt. Commun.* **280**, 492 (2007).
  - [6] C. Affeldt *et al.*, *Classical Quantum Gravity* **31**, 224002 (2014).
  - [7] M. Rakhmanov, J. D. Romano, and J. T. Whelan, *Classical Quantum Gravity* **25**, 184017 (2008).
  - [8] P. Bernard, G. Gemme, R. Parodi, and E. Picasso, *Rev. Sci. Instrum.* **72**, 2428 (2001).
  - [9] A. M. Cruise and R. M. J. Ingley, *Classical Quantum Gravity* **23**, 6185 (2006).
  - [10] T. Akutsu *et al.*, *J. Phys. Conf. Ser.* **122**, 012007 (2008).
  - [11] K. L. Dooley (LIGO Scientific Collaboration), *J. Phys. Conf. Ser.* **610**, 012015 (2015).
  - [12] B. P. Abbott *et al.* (VIRGO and LIGO Scientific Collaborations), *Nature (London)* **460**, 990 (2009).
  - [13] J. Abadie *et al.* (VIRGO and LIGO Scientific Collaborations), *Phys. Rev. D* **85**, 122001 (2012).
  - [14] J. Aasi *et al.* (VIRGO and LIGO Scientific Collaborations), *Phys. Rev. Lett.* **113**, 231101 (2014).
  - [15] J. Aasi *et al.* (VIRGO and LIGO Scientific Collaborations), *Phys. Rev. D* **91**, 022003 (2015).
  - [16] R. W. P. Drever, J. L. Hall, F. V. Kowalski, J. Hough, G. M. Ford, A. J. Munley, and H. Ward, *Appl. Phys. B* **31**, 97 (1983).
  - [17] E. D. Black, *Am. J. Phys.* **69**, 79 (2001).
  - [18] O. Kwon and C. J. Hogan, *Classical Quantum Gravity* **33**, 105004 (2016).
  - [19] C. J. Hogan and O. Kwon, [arXiv:1506.06808](https://arxiv.org/abs/1506.06808).
  - [20] C. Hogan, [arXiv:1509.07997](https://arxiv.org/abs/1509.07997); C. Hogan, O. Kwon, J. Richardson, [arXiv:1607.03048](https://arxiv.org/abs/1607.03048).